AEROELASTIC AND ACOUSTIC ANALYSIS FOR ACTIVE TWIST ROTORS

Smith Thepvongs, Carlos E. S. Cesnik
Dept. of Aerospace Engineering
The University of Michigan
Ann Arbor, Michigan, USA

Spyros G. Voutsinas
Dept. of Mechanical Engineering
National Technical University of Athens
Athens, Greece

Abstract

This paper presents an analysis framework for aeroelastic and acoustic studies of active twist rotors. An indirect tightly coupled aeroelastic solution is developed by combining a geometrically exact structural analysis with a panel method/ particle-wake aerodynamic model in the time domain. Predictions are compared with experimental data for the low-speed descent flight condition. Good agreement is obtained for elastic response, blade section normal force, and tip vortex geometry. Acoustic pressure impulses due to blade-vortex interactions are under-predicted. The effect of active twist on interaction miss distance is explored.

Introduction

Noise and vibration have been key issues in the development of modern military and commercial helicopters. A number of active control concepts, including Higher Harmonic Control (HHC) [1], active trailing-edge flap [2] and integral twist actuation [3] have demonstrated potential in reducing vibration in most flight conditions, and reducing noise caused by blade-vortex interactions (BVIs) during low-speed descent. Integral twist actuation deforms the structure directly without the use of discrete control surfaces or high-powered actuators at the swashplate. The NASA/Army/MIT Active Twist Rotor (ATR) utilizes embedded active fiber composites to provide high-frequency control of blade twist. Experiments were conducted in the NASA Langley Transonic Dynamics Tunnel using an aeroelastically scaled rotor. In open-loop tests, reduction of fixed-system vibratory loads of 60%-90% was observed, depending on flight condition [4]. Also, noise levels in the BVI flight regime were reduced by a maximum of 2.7 dB [5]. A separate CFD study showed that twist actuation could significantly reduce impulsive loading during an isolated BVI event [6].

The need to further study the effects of active twist on BVI-induced noise and vibration motivated initial work to develop a new aeroelastic/acoustic rotor simulation. This work followed existing prediction codes such as RCAS [7], DYMORE [8] and 2GCHAS [9], as well as codes developed by Friedmann et. al. [10] and ONERA [11], but included both 1) a complete structural analysis framework for blades with embedded active materials and 2) a particle-vortex, free-wake model. The general framework and methodology of this new approach were developed in previous work [12]; however, a robust implementation and strong validations were not achieved.

This paper presents the theory and development of the complete simulation for aeroelastic and acoustic analysis of active twist rotors. A validation study of aeroelastic response and aerodynamic loads is performed using experimental data from the Higher Harmonic Control Aeroacoustic Rotor Test (HART) [1]. Predictions of noise signature and parallel-BVI geometry are also compared with measurements. Twist actuation is simulated on the HART rotor configuration as a preliminary exploration of active-twist based noise reduction.

Structural Component

The basis of the structural analysis framework is the reduction of the three-dimensional, active rotor blade structure to a set of two analyses by an asymptotically correct approximation. A linear analysis is done over the 2-D cross section, and a non-linear analysis is done over the resulting 1-D beam reference line.

The cross section analysis consists of The University of Michigan's Variational Asymptotic Beam Section Analysis (UM/VABS) code [13]. This code calculates a stiffness matrix, along with mass properties and internal forces due to active materials for an arbitrary, active/passive composite material layup. The stiffness matrix calculation is based on the asymptotic solution of the warping field and takes a 4x4 matrix under Euler-Bernoulli assumptions, or a 6x6 matrix for a Timoshenko-like model. A finite-element discretization of the 2-D cross-section is used. Recovery of 3-D stress and strain can be obtained based on the values of the 1-D generalized strains determined by the beam reference line analysis. In the absence of cross

section layup information and when the stiffness and mass properties are given (as a result of experimental determination, for instance), the cross-section analysis is bypassed. This approach requires equivalent integrated internal actuation forces to be defined, and the capability to recover 3-D stress/strain is lost.

The structural dynamic analysis of the rotor reference line adopts the geometrically exact, mixed-variational formulation for the dynamics of moving beams originally presented in Ref. 14. The first-order mixed formulation is used based on the intrinsic equations of motion, and the finite-element method is used for its solution along with an implicit time integration scheme These have been implemented in UM/NLABS, Nonlinear Active Beam Solver, as described in Refs. 15 and 16.

It should be noted that recent advances have extended the theory to incorporate the effects of higher-order cross-section deformations, by assuming a set 'finite-section modes' [17]. This extension is embedded in the current solver, but the effects are assumed to be negligible in the context of the current study and are excluded in the brief presentation of the theory below.

The mixed variational formulation is derived using Hamilton's principle and can be written as

$$\int_{t_1}^{t_2}\int_0^l \left[\delta(T-U)+\delta\overline{W}\right]dx_1 dt = \delta\overline{A} \tag{1}$$

where $[t_1, t_2]$ is an arbitrary time interval, l is the length of the beam, T and U are the kinetic and internal energy densities per unit length, respectively. $\overline{\delta A}$ is the virtual action at the ends of the time interval, and $\overline{\delta W}$ is the virtual work of the applied loads per unit length. Three reference frames are defined: the B frame along the deformed beam reference line frame, the b frame along the undeformed beam reference line and the a frame representing the global rotating frame. The variation of the internal energy terms is with respect to the generalized strain column vectors, γ and κ. The variation of the kinetic energy terms is with respect to the linear velocity column vector V_B and angular velocity column vector Ω_B, with all velocities measured in the deformed blade frame B. F_B and M_B are the internal force and moment column vectors and P_B and H_B are the linear and angular momenta column vectors. These are defined in the B frame as:

$$F_B = \left(\frac{\partial U}{\partial \gamma}\right)^T, M_B = \left(\frac{\partial U}{\partial \kappa}\right) \tag{2}$$

$$P_B = \left(\frac{\partial T}{\partial \kappa}\right)^T, H_B = \left(\frac{\partial T}{\partial \kappa}\right)^T \tag{3}$$

The first element of F_B is the axial force and the second and third elements are the shear forces. Similarly, the first element of M_B is the twisting moment and the second and third elements are the bending moments.

The following constitutive equations relate the generalized strain and force measures, and the velocity and momenta measures:

$$\begin{bmatrix} F_B \\ M_B \end{bmatrix} = [K]\begin{bmatrix} \gamma \\ \kappa \end{bmatrix} - \begin{bmatrix} F_B^{(a)} \\ M_B^{(a)} \end{bmatrix} \tag{4}$$

$$\begin{bmatrix} P_B \\ H_B \end{bmatrix} = [M]\begin{bmatrix} V_B \\ \Omega_B \end{bmatrix} \tag{5}$$

The actuation forces and moments, $F_B^{(a)}$ and $M_B^{(a)}$, depend on the geometry, material distribution and applied electric field. The stiffness matrix [K], mass matrix [M] and actuation vector are provided by the cross-section analysis when the material and geometry details are known.

The geometrically exact kinematical relations are given in the member frame, with rotations represented by Rodrigues parameters, θ:

$$\gamma = C^{Ba}(C^{ab}e_1 + u_a') - e_1 \tag{6}$$

$$\kappa = C^{ba}\left(\frac{\Delta - (\tilde{\theta}/2)}{1+(\theta^T\theta/4)}\right)\theta' \tag{7}$$

$$V_B = C^{Ba}(v_a + \dot{u}_a + \tilde{\omega}_a u_a) - e_1 \tag{8}$$

$$\Omega_B = C^{ba}\left(\frac{\Delta - (\tilde{\theta}/2)}{1+(\theta^T\theta/4)}\right)\dot{\theta} + C^{Ba}\omega_a \tag{9}$$

where the notation C^{pq} represents, for example, the rotation matrix from frame q to frame p, u_a is the displacement vector in the a frame, Δ is the 3x3 identity matrix, v_a and w_a are the initial velocity and initial angular velocity of a point on the a frame and e_1 is the unit vector $[1,0,0]^T$. $\dot{u}_a$ and $\dot{\theta}_a$ are the time derivatives of displacement and rotation, u_a' and θ' are the derivatives with respect to the spanwise curvilinear coordinate. The mixed formulation is derived by using Lagrange multipliers to enforce the kinematical equations. A transformation is performed such that all δ quantities, displacement, and rotation are measured in the global frame a and the strains, velocities, forces, and momenta are measured in the deformed reference frame B. The a frame version of the variational formulation was derived in Ref. 18.

The spatial finite element discretization uses linear shape functions due to the weak form of the variational formulation. The resulting time-domain non-linear equations are expressed as:

$$F_S(X,\hat{X}_{x=0},\hat{X}_{x=1})+A(X)\cdot\dot{X} \\ -F_L(X,\hat{X}_{x=0},\hat{X}_{x=1})=0 \qquad (5)$$

where A is the inertial operator, F_S is the structural operator, F_L is the load operator and the actuation forces, $F_B^{(a)}$ and $M_B^{(a)}$, are time dependent and associated with F_S. X is the state vector at each element, containing the vectors of displacements, forces and momenta, with $\hat{X}$ representing the boundary element values. Solution of equation (5) is obtained by time integration using the second order backward Euler method, and Newton-Raphson iteration to solve the resulting set of nonlinear algebraic equations. The Jacobian matrix is defined analytically, with the full expressions given in Ref. 3.

Several updates have been made to the code as part of the current work which focuses on rotor blade analysis. Non-linear torsional stiffness due to axial loads is considered by continuous update of the stiffness value according to Ref. 19. Also, the rigid-body velocity associated with rotation of the undeformed B frame with respect to the global rotating b frame has been included to account for pitch control.

Aerodynamic Component

The GENUVP aerodynamic code, developed at the National Technical University of Athens (NTUA), uses a panel method with a particle vortex approximation for the wake. This approach allows for high-resolution of the wake with a moderate computational cost. A detailed description is provided in Ref. 20. A brief overview is presented here. GENUVP is based on the Helmholtz decomposition theorem, which allows the flowfield to be split into an irrotational part ($\vec{u}_{solid}$) representing the presence of solid boundaries and a rotational part which includes the wake influence ($\vec{u}_{wake}$). Considering an arbitrary external flow ($\vec{u}_{ext}$), the velocity field can be described by:

$$\vec{u}(\vec{x},t)=\vec{u}_{ext}(\vec{x},t)+\vec{u}_{solid}(\vec{x},t)+\vec{u}_{wake}(\vec{x},t) \qquad (6)$$

where $\vec{x}$ is a position inside the flowfield and t is the time.

Green's theorem allows the presence of solid boundaries to be expressed through surface singularity distributions, suggesting the use of a panel method. Lifting bodies can be modeled using a thin or thick representation: thin bodies are comprised of dipole distributions along the camber line; thick bodies use a combination of dipoles and sources distributed along the lifting surface. For the present study, the thick representation was found to be essential for resolving the surface pressures needed for acoustics computations. A tip closure is constructed of dipole panels.

At each time step, a near wake is formed as a result of satisfying the Kutta condition along the trailing edge and at selected intersections along the tip edge. The near wake retains a surface character for the current time step. Figure 1 shows the near wake at a single timestep, along with the panel geometry for a typical rotor blade using the thick representation. At the subsequent time step, the surface vorticity is integrated to form vortex particles.

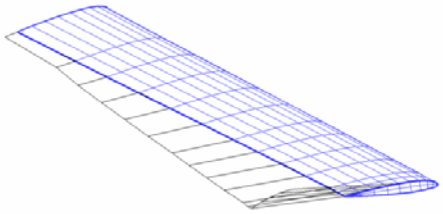

Figure 1. Typical panel geometry and near wake

In the current application, the velocity associated with the particles has been regularized following Beale and Majda [21]:

$$\vec{u}_{wake}(\vec{x},t)=\sum_{m}^{N}\frac{\vec{\Omega}_m(t)\times\vec{R}_m}{4\pi R_m^3}\left[1-\exp(R_m/\varepsilon)^3\right] \qquad (7)$$

where $\vec{R}_m$ is the position vector from the particle m to $\vec{x}$, $\vec{\Omega}_m$ is the intensity vector of particle m and N is the total number of particles at t. ε denotes the cut-off length associated to the numerical scales determined by the time step and grid size of the paneling.

The vortex particles are convected with the local velocity at the current time, and are also subject to vortex stretching. The changes in position, $\vec{Z}_m$, and intensity are respectively given by:

$$\frac{d\vec{Z}_m}{dt}=\vec{u}\left(\vec{Z}_m,t\right) \qquad (8)$$

$$\frac{d\vec{\Omega}_m}{dt}=\left(\vec{\Omega}_m\nabla\right)\vec{u}\left(\vec{Z}_m,t\right) \qquad (9)$$

The particles are formed from all near wake elements. Although the inclusion of inboard vortices results in a sizeable numerical representation of the free vorticity, this gives the most complete representation of the rotor wake. This is important because the formation of secondary vortices due to negative tip loading has been observed during the HART experiments [1].

A visualization of the particle-vortex wake is shown in Figure 2 for a descent flight condition.

The section aerodynamic forces along the rotor blades are calculated by direct integration of the panel pressures, which are given by the unsteady form of Bernoulli's equation. This method excludes the effects of static or dynamic stall, which are taken to be negligible in the test cases studied. Steady viscous drag is calculated using tabulated data based on effective angle of attack.

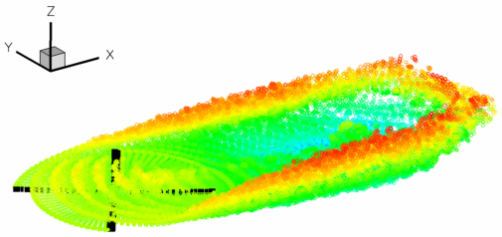

Figure 2. Visualization of BO105 rotor wake, low-speed descent

Acoustic Component

The current model incorporates an acoustics solver based on the Farassat 1A solution of the Ffowcs Williams-Hawkings (FW-H) acoustic analogy. The analogy approach allows the acoustic pressure to be calculated at a far-field location using quantities determined locally at the body surface. The Farassat 1A solution is derived by integration over the body surface, with the integrals evaluated at the emission time. The solution for the thickness and loading noise is first presented in [22], and shown in its complete form in [23]. In the absence of compressibility effects, the total noise is dominated by the sum of the thickness and loading noise [23]. The current implementation uses a discrete form, with each aerodynamic panel representing a source of thickness and loading noise. A source-time dominant approach is taken, therefore a time interpolation is performed to determine the acoustic pressure at fixed observer time intervals.

Aeroelastic Coupling

The aerodynamic and structural components maintain separate discretizations of the rotor blades. The structural analysis divides the beam reference line into 1-D beam elements, and the aerodynamic analysis models the surface with panel elements that constitute a 3-D aerodynamic mesh. For a typical blade, the beam reference line in 3-D space intersects the quarter-chords of the mean lines defining the strips of aerodynamic nodes, since the cross section properties are usually taken about this location. The current implementation requires that for every strip of aerodynamic nodes there be a spanwise coincident structural node and also an additional structural node centered in between. The additional computational cost associated with using more structural elements is negligible compared to that of the aerodynamic calculations. This method avoids interpolation of the structural displacements, velocities and aerodynamic forces. The structural displacements are used to deform the strips of aerodynamic nodes, while the velocities are needed at the panel centers to define the non-entry boundary conditions in the aerodynamics. The aerodynamic forces are also taken at the panel centers.

It should be noted that rotations of the strips of aerodynamic nodes are performed using rotation matrices as defined by the Rodrigues parameters describing the rotation degrees of freedom in the structural solution. Also, all three integrated aerodynamic forces and moments are considered. As a result, the accuracy for large displacements and rotations is preserved in the coupled aeroelastic solution.

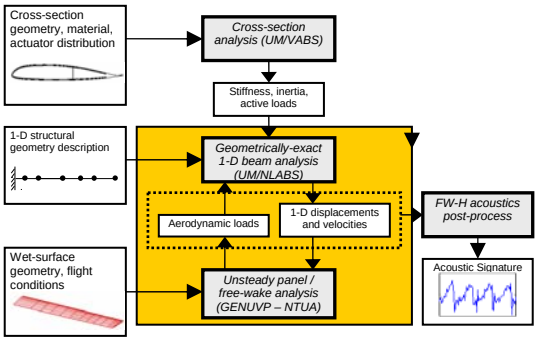

Figure 3. Framework for aeroelastic and acoustic analysis of active twist rotors

A flowchart of the aeroelastic simulation is shown in Figure 3. Solutions of the aerodynamic and structural components are obtained separately, with exchanges of aeroelastic information done at every time step. This aeroelastic coupling method can be classified as tightly coupled and indirect. The aerodynamic solution is obtained based on the deformed blade position and structural velocity calculated at the previous time step. This solution is used in the acoustic calculation, and in obtaining the aerodynamic loads. The loads are then passed to the structures code, which solves for the new position and velocity.

The trimmed solution of the control settings is determined by the Newton Raphson method, using the full-resolution, time-domain aeroelastic solution. The time-averaged body-fixed loads at the hub are calculated once the response is periodically converged. The Jacobian is calculated numerically by small pertubations of the individual control settings. For the test cases presented in this study,

convergence of the trim solution within two iterations was observed.

BO105 Model Development

The HART data used in this study corresponds to a 5.3° descent flight condition at advance ratio μ = 0.15. The scaled BO105 rotor is four-bladed and has a radius of 2.0 m and chord of 0.121 m. In the current rotor blade model, stiffness and mass properties were substituted using data obtained from measurements [24]. The effects of elastic axis and center of gravity offset from the reference line are included by adjustments to the off-diagonal terms of the mass and stiffness matrices according to Ref. 25. This method is valid when material-induced bend-twist coupling is not present, as assumed for the HART rotor blades.

The aerodynamic grid consists of 16 spanwise panels, concentrated near the tip, and 26 chordwise panels (13 on upper surface, 13 on lower surface), concentrated near the leading edge. A set of panels also closes the tip. The near wake emerges from the trailing edge of all sections. Also, additional near wake elements are created at the junction between the upper surface and tip closure surface, along the five shared panel edges closest to the trailing edge. The rotor azimuth increment between time steps is 4°.

Elastic Tip Response and Normal Force

Calculations for the elastic response at the blade tip are shown in Figure 4 along with HART measurements for the baseline, HHC minimum noise (MN) and HHC minimum vibration (MV) test cases. Close agreement is obtained in the phase and frequency of the flap response for all test cases. The peak-to-peak amplitude is captured accurately for the baseline case, but slightly over-predicted in the HHC results. In the baseline twist response, significant error is present with predictions containing a 4/rev component not present in the experimental data. It should be noted that difficulty in capturing the HART baseline twist response has been observed in other computational studies [9-11]. For the HHC twist response, the dominant 3/rev frequency is captured with small errors in phase and amplitude.

A comparison of measured and predicted blade section normal force at 0.87R is shown in Figure 5. The low-frequency variation is predicted with close agreement for the HHC cases. For the baseline calculation, reduced amplitude is shown on the retreating side, which is consistent with the discrepancy in the twist response. The impulsive loading due to BVIs in the first and fourth quadrants is present in the calculations for all test cases, but with smaller amplitude compared to the experimental data.

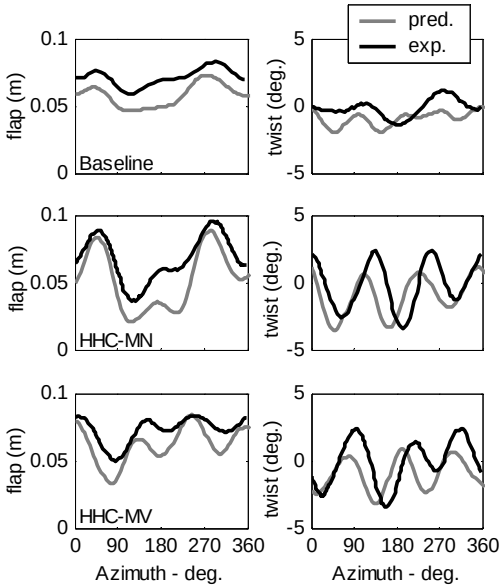

Figure 4. HART elastic tip response

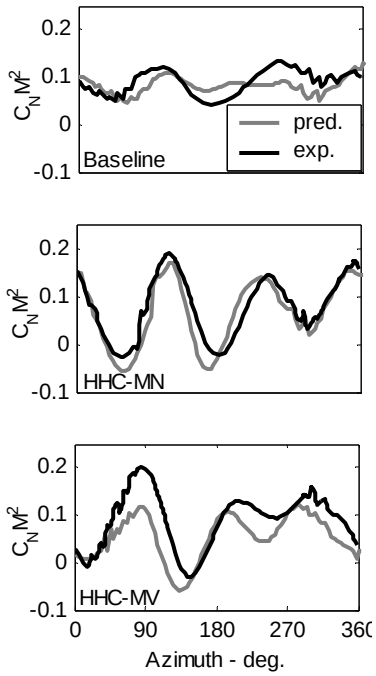

Figure 5. HART normal force

Acoustic Pressure

The acoustic pressure results are given at the experimentally-determined noisiest locations on the advancing and retreating side, 2.0 m below the rotor plane. The experimental results are shown in Figure 6 and the predictions are shown in Figure 7. The correlation is reasonable for the low-frequency variation, but the strong high-frequency impulses associated with BVI events are not present in the calculations. Several attempts were made to improve the resolution of the pressure spikes, including reduction of the simulation azimuth increment from 4.00° to 1.25°, increasing the panel density and perturbation of the flight path angle. These changes were not found to have a substantial effect on the high-amplitude spikes in the trimmed solution.

Geometry of Individual Interactions

The position of the tip vortex was estimated by tracking the time-series of a particle shed from the tip-edge of each blade. Since the actual tip vortex formation is constituted by a collection of vortex particles, some shed at locations slightly inboard, the true tip vortex center is not defined exactly by the particles shed from the tip edge. It is assumed that the tip edge particles represent a close approximation when a small amount of time has elapsed after emission.

For the results given below, a reduced grid size of 12 spanwise panels and 21 chordwise panels was used, with a 4° azimuth increment. No significant changes in the tip vortex position were observed compared to the higher resolution model.

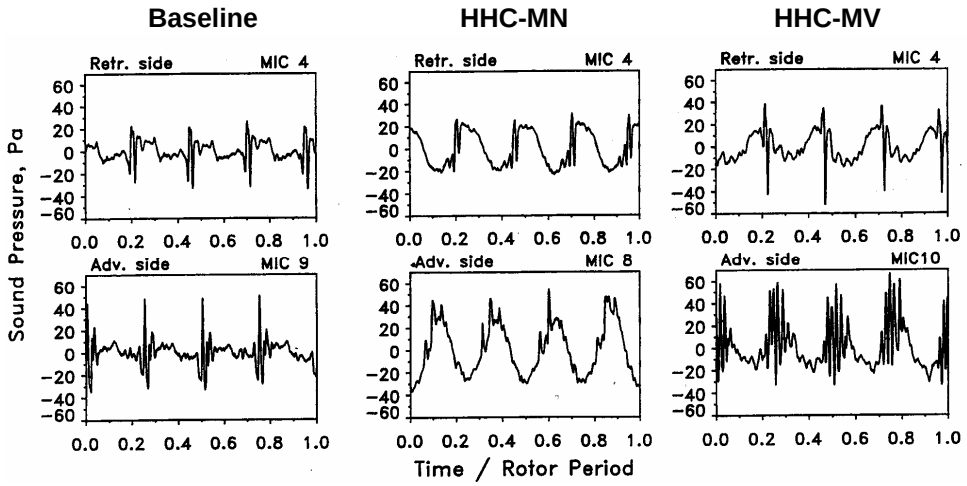

Figure 6. Experimental HART acoustic signature at noisiest locations

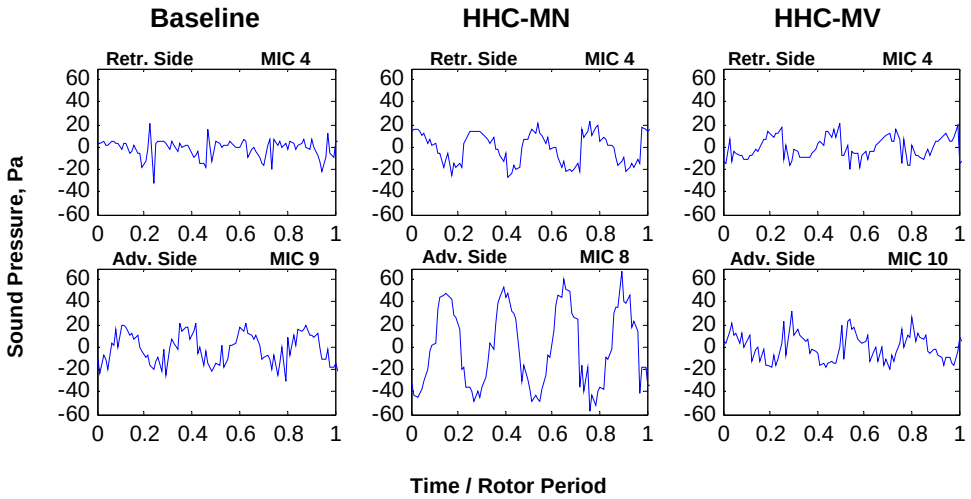

Figure 7. Predicted HART acoustic signature at noisiest locations [1]

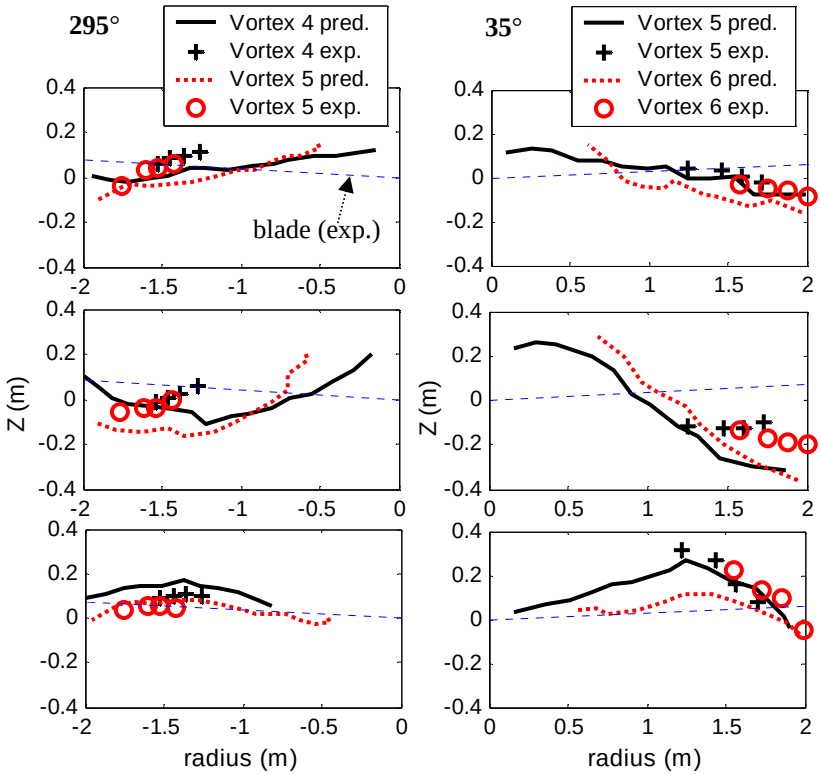

Figure 8. HART vortex out-of-plane position at 295° and 35° azimuthal positions

Figure 8 shows the geometry of the most parallel BVIs in the vertical plane for the advancing and retreating side. The snapshots are taken when the blade is at 35° azimuth for the advancing side, and 295° for the retreating side. The view is along the plane of the rotor, and perpendicular to the blade in the plane. Experimental data was obtained by the Laser Light Sheet (LLS) technique [1]. The calculated results represent data interpolated between two successive time steps since the simulation azimuth positions did not include 35° and 295°.

For the advancing side, the measurements show a small miss distance and out-of-plane interaction angle for the baseline case, which are reproduced by the calculations. The calculations give slightly lower vortex positions than the measurements. Under HHC-MN actuation, the miss distance increases significantly as the tip vortices move downward in the experiment. This effect is observed in the calculation, but the computed miss-distance is greater. Also, the tip vortex inclination at 0.75R is larger in the calculations, which may be due to an under-prediction of the tip-vortex movement inward along the span. The HHC-MV test case shows close correlation in the position and inclination of vortex #6, but with some discrepancy in both quantities for vortex #5.

The retreating side measurements and predictions show a smaller effect of HHC on the tip vortex geometry. The slight downward shift of the vortex position in the HHC-MN case, and the slight upward shift of the vortex position in the HHC-MV case are given by the predictions similar to the measurements. Overall, the trend of vortex position changes due to HHC is captured well for the advancing and retreating side samples, although there are differences in the absolute positions.

Simulated Active Twist

Due to problems in resolving the BVI-induced impulses in the noise signature, the active twist study considers as an alternative the effects on the interaction geometry. This is justified by the fact that the miss distance was found to have the largest impact on rotor noise in the HART experiment, with blade unloading and interaction vortex strength being of secondary importance [1]. The HART rotor configuration is used as a platform for simulated active twist in order for comparisons to be made with baseline and HHC data. Effective internal moments due to simulated active twist are applied to the HART structural model, consistent with eq. (2). Only the spanwise blade region which has a full airfoil section is considered active (outboard of 22% span), following the NASA/Army/MIT ATR design

[26]. Actuation moments are constant along the span and the magnitude is specified to match the static tip twist of +/-0.5° achieved in the ATR. Using this actuation moment magnitude, the dynamic tip twist at 3/rev was computed to be +/-1.15° under rotation in vacuum, compared to +/-1.0° observed in the ATR during forward-flight wind tunnel testing [4]. It should be noted that recent design-analysis studies optimizing the ATR structure suggest that significantly greater twist amplitudes can be achieved [27].

An actuation frequency of 3/rev was considered in this preliminary investigation since 3/rev was found to be the most effective in noise reduction during the HART experiments. Also, it was presumed that the twist actuation would be capable of producing similar aerodynamic effects as HHC. The active twist phase angle for maximum advancing side miss distance of vortex #5 at 0.75R was located by a manual bisection method within a 15° range. This phase angle was found to be Ψ_c = 116°, compared to the HHC-MN actuation of 296° (at 3/rev). A comparison of the vortex #5 positions at selected control phase angles is shown in Figure 9. A clear influence on the vertical positions is observed. In Figure 10, the baseline and the active twist prediction for the 116° control phase are provided for both the advancing and retreating sides, and for both vortex pairs. On the retreating side, a small downward shift is observed similar to the HHC results. For the advancing side, the downward displacements of the tip vortices are approximately 50% of those achieved by HHC at 0.75R.

The elastic flap and twist response at the tip are shown in Figure 11 for the same actuation phase angles as Figure 9. Although the twist actuation phase has a significant effect on flap response, at 35° azimuth (the location of the blade when the advancing side vortex positions are recorded), only small changes are observed. Both the twist and flap response using the 116° control phase matches that of HHC-MN (Figure 4), with a reduced amplitude. An interesting occurrence is the increase of the maximum amplitude to +/-2.13° for the 116° control phase in comparison with the twist at other phase angles. These results indicate that the aerodynamic moments are approximately in phase with the actuation schedule in the case of greatest miss distance.

Figure 12 compares the tip pitch response of active twist scheduled at Ψ_c = 116° and the HHC-MN predictions. The pitch measurement includes elastic twist and, for the HHC-MN case, the 3/rev pitch inputs. The results show that the responses are similar with only slightly larger amplitude induced by HHC. This suggests that the larger downward convection of the tip vortices produced

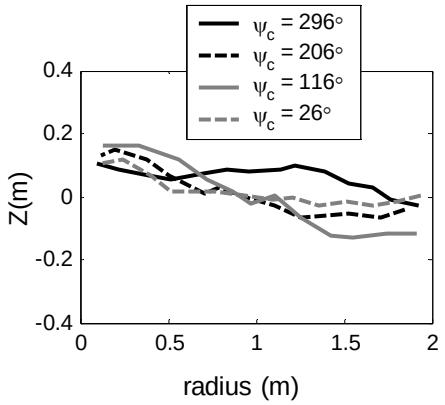

Figure 9. Vortex 5 positions for active twist at various actuation phase angles

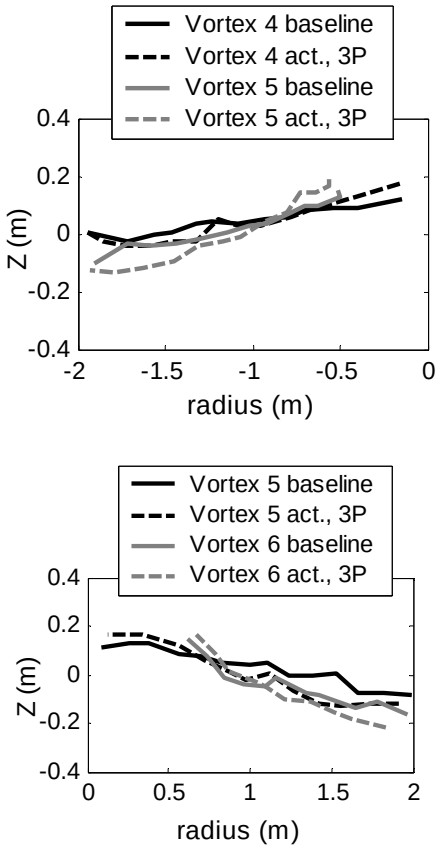

Figure 10. Comparison of vortex positions for baseline and simulated active twist (Ψ_c = 116°)

by HHC in this study may be due to the greater pitch rotations achieved at inboard locations compared to active twist. This, however, has to be further investigated.

The preliminary results obtained from the active twist numerical study indicate that twist actuation is capable of modifying BVI geometry. Although the general effect is smaller compared to HHC, the case considered uses conservative actuation moments simulated on the HART platform. It is expected that larger induced twist deflections, as predicted for recent optimized designs [27], will significantly increase the influence on the miss distance.

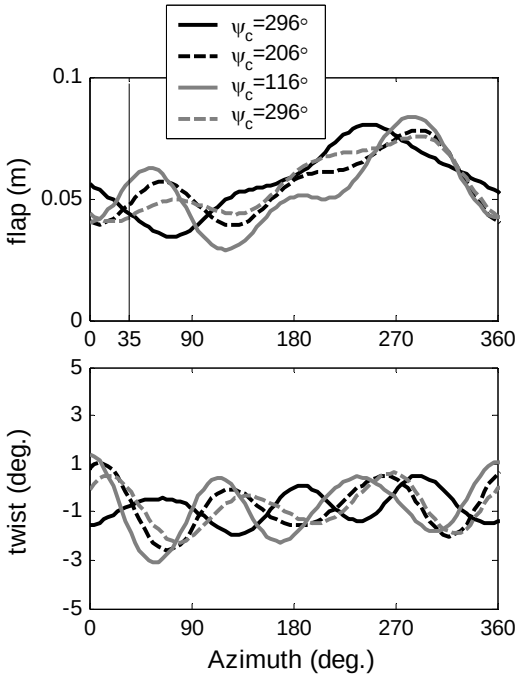

Figure 11. Elastic tip response for 3/rev active twist control

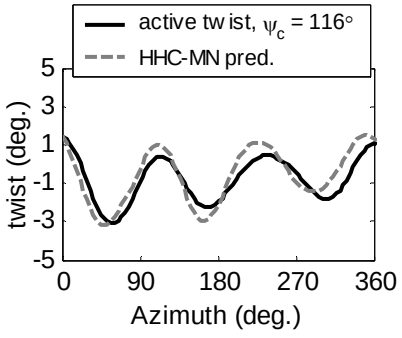

Figure 12. Total tip pitch response, components above 1/rev.

Conclusions

A closely coupled aeroelastic solution has been developed by combining a geometrically exact beam solver with a panel method/particle-wake code. Aeroelastic response and low-frequency load prediction is shown to have good correlation with experimental data. Difficulty in capturing impulsive loading due to blade-vortex interactions is observed, particularly in the acoustic signature. A preliminary investigation regarding the use of active twist technique to mitigate noise was conducted. The study simulated 3/rev twist actuation and demonstrated effectiveness in increasing blade-vortex miss distance. A more extensive study examining other noise reduction mechanisms, using a greater range of actuation frequencies, should be considered. Improvements on the acoustic prediction will be required to fully assess active-twist-based noise reduction.

Acknowledgements

This work has been sponsored in part by the Army Research Office (grant 43854-EG) with Dr. Gary L. Anderson as the technical monitor.

References

1. Splettstoesser, W., Seelhorst, U., Wagner, W., Boutier, A., Micheli, F., Mercker, E., and Pengel, K. , "Higher Harmonic Control Aeroacoustic Rotor Test (HART) – Test Documentation and Representative Results," DLR Report IB 129-95/28 and appendices, December 1995.

2. Friedmann, P.P, "Vibration Reduction in Rotorcraft Using Actively Controlled Flaps – From Theoretical Concept to Flight-Ready Hardware," Proceedings of the AHS 4th Decennnial Aeromechanics Specialist's Conference, San Francisco, California, January 2004.

3. Cesnik, C.E.S., Shin S-J, Wilkie, W.K., Wilbur, M.L. and Mirick, P.H., "Modeling, Design and Testing of the NASA/Army/MIT Active Twist Rotor Prototype Blade," Proceedings of the American Helicopter Society 55th Annual Forum, Montreal, Canada, May 1999.

4. Wilbur, M.L., Mirick, P.H., Yeager Jr., W.T., Langston, C.W., Cesnik, C.E.S and Shin, S., "Vibratory Loads Reduction Testing of the NASA/Army/MIT Active Twist Rotor", *Journal of the American Helicopter Society*, Vol. 47, No. 2, April 2002

5. Booth Jr., E.R. and Wilbur, M.L., "Acoustic Aspects of Active-Twist Rotor Control," *Journal of the American Helicopter Society*, Vol. 49, No. 1, January 2002.

6. Chen, P.C., Baeder, J.D., Evands, R.A.D and Niemczuk, J., “Blade-vortex interaction noise reduction with active twist smart rotor technology,” *Smart Materials and Structures 10*, pp. 77-85, 2001.

7. Saberi, H., Khoshlahjeh, M., Ormiston, R**.** and Rutkowski, M. "Overview of RCAS and Application to Advanced Rotorcraft Problems," Proceedings of the American Helicopter Society 4th Decennial Specialists' Conference on Aeromechanics, San Francisco, California, January 21-23, 2004.

8. Bauchau, O.A., “Computational Schemes for Flexible, Non-Linear Multi-Body systems,” *Multibody Systems Dynamics*, Vol. 2, No. 2, 169-225, 1998.

9. Lim, J.W., Tung, C., and Yu, Y.H., “Prediction of Blade-Vortex Interaction Airloads with Higher-Harmonic Pitch Controls Using the 2GCHAS Comprehensive Code”, *Journal of Pressure Vessel Technology*, Vol. 23, November 2001.

10. Liu, L., Patt. D., and Friedmann, P.P., “Simultaneous Vibration and Noise Reduction in Rotorcraft Using Aeroelastic Simulation,” Proceedings of the AHS 60th Forum, Baltimore, Maryland, 2004.

11. Beaumier, P. and Delrieux, Y., “Description and Validation of the ONERA Computational Method for the Prediction of Blade-Vortex Interaction Noise”, ONERA TP 2003-141.

12. Cesnik, C., Opoku, D., Nitzsche, F. and Cheng, T., “Active Twist Rotorblade Modelling using Particle Wake Aerodynamics and Geometrically-exact Beam Structural Dynamics,” *Journal of Fluids and Structures 19*, 651-668, 2004.

13. Cesnik, C.E.S. and Hodges, D. H.: "VABS: A New Concept for Composite Rotor Blade Cross-Sectional Modeling*," Journal of the American Helicopter Society*, Vol. 42, No. 1, Jan. 1997.

14. Hodges, D.H., “A mixed Variational Formulation Based on Exact Intrinsic Equations for Dynamics of Moving Beams,” *International Journal of Solids and Structures* 26, pp. 1253-73, 1990.

15. Palacios, R, Cesnik, C.E.S., “Structural Dynamics of Integrally Strained Slender Wings,” International Forum of Aeroelasticity and Structural Dynamics, Amsterdam, The Netherlands, June 2003.

16. Palacios, R., “Asymptotic Models of Integrally-Strained Slender Structures for High-Fidelity Nonlinear Aeroelastic Analysis,” Ph.D. Thesis, The Unversity of Michigan, 2005.

17. Palacios, R and Cesnik, C.E.S., “Reduced Structural Modeling of Integrally-Strained Slender Wings,” 45th AIAA/ASME/ASCE/AHS/ASC Structures, Structural Dynamics and Materials Conference, Palm Springs, California, Apr. 19-22, 2004.

18. Shang, X., “Aeroelastic Stability of Composite Hingeless Rotors with Finite-State Unsteady Aerodynamics”, Ph.D. Dissertation, Georgia Institute of Technology, Atlanta, Georgia, 1995.

19. Atilgan, A.R. and Hodges, D.H., “Unified Nonlinear Analysis for Nonhomogeneous Anisotropic Beams with Closed Cross Sections,” *AIAA Journal*, Vol. 29, No. 11, 1991.

20. Voutsinas, S.G. and Triantos, D.G., “High Resolution Aerodynamic Analysis of Full Helicopter Configurations,” 25th European Rotorcraft Forum, Rome, Italy, 1999.

21. Beale, J.T. and Majda, A., “High Order Accurate Vortex Methods with Explicit Velocity Kernels,” *Journal of Computational Physics*, Vol. 58, pp. 188-208, 1985.

22. Farassat, F., Succi, G.P., “The prediction of helicopter rotor discrete frequency noise,” Vertica, Vol. 7, No. 4, pp. 309-320, 1983.

23. Brenter, K.S., Prediction of Helicopter Rotor Discrete Frequency Noise - a Computer Program Incorporating Realistic Blade Motions and Advanced Acoustic Formulation, NASA-TM-87721, 1986.

24. Burley, C., HART II pre-test data, Personal communication via Cesnik, C.E.S., 2003.

25. Yu, W., Volovoi, V.V., Hodges, D.H. and Xianyu, H., “Validation of the Variational Asymptotic Beam Section Analysis (VABS),” *AIAA Journal*, Vol. 40, No. 10, October 2002.

26. Cesnik, C.E.S., Shin, S-J,Wilbur, M.L., “Dynamic response of active twist rotor blades,” Smart Materials and Structures *Smart Materials and Structures 10*, pp. 62-76, 2001.

27. Cesnik, C. E. S., Mok, J., Morillo, J. A., and Parikh, A., “Design Optimization of Active Twist Rotor Blades,” 30th European Rotorcraft Forum, Marseille, France, September 16—18, 2004.